Alkali-metal ions (M^+ = Li^+, Na^+, K^+, Rb^+, and Cs^+) endohedral cyclo[18]carbon (C_{18}): Exploring binding interactions and predicting optical properties

Yang Xiao [a], Yinling Xiao [a], Xia Wang [a], Yixiao Chen [b], Xiufen Yan [a], Zeyu Liu [a,*], Tian Lu [c,*]

[a] *School of Environmental and Chemical Engineering, Jiangsu University of Science and Technology, Zhenjiang 212100, People's Republic of China*

[b] *College of Life Science and Chemistry, Jiangsu Second Normal University, Nanjing 210013, People's Republic of China*

[c] *Beijing Kein Research Center for Natural Sciences, Beijing 100022, People's Republic of China*

Abstract

With growing interest in carbon-based materials for energy storage and active research in the field of advanced optoelectronic devices, we theoretically designed ten complexes by cyclo[18]carbon (C_{18}) inside and outside complexing alkali-metal ions (M^+ = Li^+, Na^+, K^+, Rb^+, and Cs^+), respectively referred to as $M^+@C_{18}^{in}$ and $M^+@C_{18}^{out}$, and performed careful analyses of binding interaction between M^+ and C_{18} as well as optical properties of stable endohedral complexes $M^+@C_{18}^{in}$. The effects of atomic number of alkali-metals on electronic structures, binding interactions, electronic absorption spectra, and molecular (hyper)polarizabilities of the $M^+@C_{18}^{in}$ were studied using accurate density functional theory (DFT) calculations. The research results indicated that the differences in radius and properties of M^+ lead to different binding modes and strengths with C_{18}, but there is no difference in electronic absorption spectra between the complexes; the polarizability and second

* Corresponding authors. E-mail addresses: liuzy@just.edu.cn (Z. Liu), sobereva@sina.com (T. Lu).

hyperpolarizability of $M^+@C_{18}^{in}$ containing different alkali-metal ions are similar due to their analogous electronic structures, but their first hyperpolarizability differ greatly due to discrepancies in molecular symmetry. The similarities and differences in intramolecular interactions, electronic absorption spectra, and (hyper)polarizability of $M^+@C_{18}^{in}$ were explored using advanced wavefunction analysis methods.

Keywords: alkali-metal ions, cyclo[18]carbon, binding interaction, electronic absorption spectrum, (hyper)polarizability

1. Introduction

Lithium ion (Li^+) batteries (LIBs) play a vital role in various electronic devices in today's society,[1] but the limited and uneven distribution of lithium resources makes them difficult to meet the needs of large-scale applications. For this reason, batteries based on earth-abundant alkali-metals, also known as "post LIBs", have been proposed as alternatives,[2-7] and the discovery of anode materials suitable for various alkali-metal ion batteries (AMIBs) has become an important topic in scientific community. Carbonaceous electrode materials, including pure/doped/hybrid forms of carbon nanomaterials with sp^2-hybridization such as fullerenes, graphene, and carbon nanotubes, are attracting significant attention as promising anode candidates for AMIBs. The recent report by Kothandam et al. reviewed latest overview of these advanced carbon-based structures in energy storage and conversion.[8]

Cyclocarbon is a new carbon allotrope, composed of carbon atoms holding hands. Earlier intermittent research on such carbon molecules provided only evidence of their existence in the gas phase.[9-12] In 2019, the successful generation and clear imaging of cyclo[18]carbon (C_{18}) in condensed phase quickly sparked a research boom on cyclocarbons.[13] Subsequently, in the past four years, due to its attractive aesthetic structure and potential application prospects, a large number of property predictions and synthesis attempts for C_{18} and its analogues were emerged.[14-47] Thereinto, our group has conducted extensive and in-depth theoretical research on C_{18} ring and related systems, and achieved significant results.[29-44] Very recently, three smaller carbon rings, i.e., cyclo[16]carbon (C_{16}),[46] cyclo[14]carbon (C_{14}),[47] and cyclo[10]carbon (C_{10}),[47] have also been prepared and characterized in the condensed phase, which is bound to trigger another wave of research enthusiasm for cyclocarbons.

Although scientific research has achieved dazzling achievements in both the storage of alkali-metal ions (M^+ = Li^+, Na^+, K^+, Rb^+, and Cs^+) and the preparation of cyclocarbon molecules, the use of cyclocarbons for energy storage has not been reported. The exploration of the properties of materials formed by M^+ doped cyclocarbons is therefore also blank.

Toward a deep understanding of the performances of bulk materials, the first step should be to study the structure and properties of their constituent molecules. Based on the analyses of the above research status, here we designed ten complexes $M^+@C_{18}$ of M^+ endohedral and exohedral C_{18}, respectively denoted by $M^+@C_{18}^{in}$ and $M^+@C_{18}^{out}$, and conducted in-depth studies of interaction of M^+ with C_{18} as well as optical properties of stable endohedral configurations. The purpose of this work is to investigate theoretically the utility of cyclocarbons for alkali-metal ion storage and the possibility of the formed complexes as optoelectronic functional materials.

2. Computational details

Geometry optimizations of the $M^+@C_{18}$ were performed by density functional theory (DFT) using *ω*B97XD exchange-correlation functional[48] in conjunction with ma-TZVP basis set.[49,50] Vibrational frequency analyses were subsequently conducted on the optimized geometries to determine that they are stable structures on the potential energy surface (PES).

Gibbs free energies *G*(X) of the $M^+@C_{18}$ were evaluated by summing up the fairly accurate single point energies *E*(X) of *ω*B97X-V[51]/def2-QZVPP[52] level in combination with Counterpoise correction and the thermal corrections to free energy obtained via frequency analysis. Natural population analyses (NPA) and Wiberg bond order (calculated based on natural atomic orbitals) of the $M^+@C_{18}^{in}$ were calculated based on *ω*B97XD/ma-TZVP wavefunctions. Electron excitations were investigated by means of the time-dependent DFT (TD-DFT) method at *ω*B97XD/ma-TZVP level at optimized ground-state geometries. Charge-transfer spectra (CTS)[32] were plotted based on the TD-DFT results. The *ω*B97XD functional combining with very large d-aug-cc-pVTZ(-PP) basis sets[53,54] within the framework of DFT were employed for calculating optical nonlinearity and (hyper)polarizability density of the $M^+@C_{18}^{in}$.

All quantum chemistry calculations were carried out by Gaussian 16 (A.03) program package,[55] except for high-level single-point energy calculations performed using ORCA 4.2.1.[56] High order symmetry-adapted perturbation theory (SAPT) analysis by SAPT2+(3)δMP2 method in conjunction with def2-TZVP basis set for

gaining deeper insight into the interaction energy was accomplished in PSI4 1.3.2 code.[57] The analyses of electronic wavefunction and the presentation of CTS were finished by Multiwfn 3.8(dev) code.[58] The isosurface maps of molecular orbitals (MOs), hole and electron, and (hyper)polarizability density, as well as the unit sphere representation of (hyper)polarizability were all rendered by using Visual Molecular Dynamics (VMD) software[59] based on the related files exported by Multiwfn.

3. Results and Discussion

3.1 Geometric Structure, Energy, and Electronic Structure of $M^+@C_{18}^{in}$

The optimized geometries of complexes $M^+@C_{18}^{in}$ and $M^+@C_{18}^{out}$ are displayed in Figure 1, and the Cartesian coordinates of them are listed in Tables S1 and S2, respectively. As seen from the relative free energy (ΔG) and equilibrium constant ($K^{in/out}$) at standard ambient condition in Table 1, the endohedral complexes $M^+@C_{18}^{in}$ are significantly lower in energy compared to their respective exohedral counterparts, and the relative energies of two configurations increase with the atomic number of the alkali-metal, indicating that M^+ are more inclined to adsorb inside the C_{18} ring, and the higher the atomic number, the more pronounced this trend becomes. Based on this, our subsequent discussions in this paper will focus on M^+ endohedral C_{18}, that is, $M^+@C_{18}^{in}$, only.

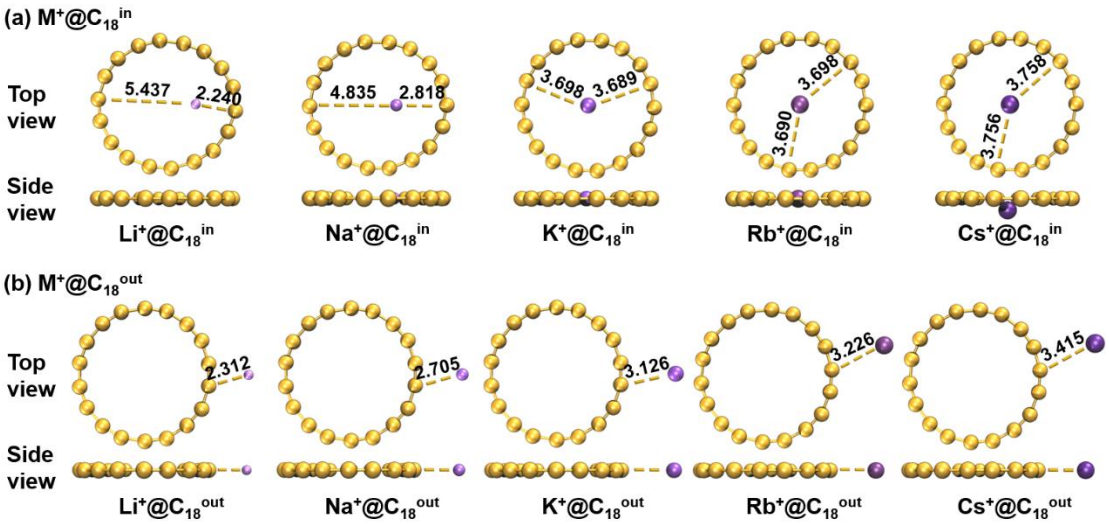

Figure 1. Optimized structures of complexes (a) $M^+@C_{18}^{in}$ and (b) $M^+@C_{18}^{out}$. The labelled distances are in Å.

Table 1 Absolute free energy (G^{in} and G^{out}, in a.u.), relative free energy (ΔG, in kcal mol^{-1}), and equilibrium constant ($K^{in/out}$) of complexes $M^+@C_{18}^{in}$ and $M^+@C_{18}^{out}$ at standard ambient condition

	G^{in}	G^{out}	ΔG^a	$K^{in/out b}$
$Li^+@C_{18}$	-692.60559	-692.60347	1.3	9.4
$Na^+@C_{18}$	-847.37016	-847.36763	1.6	14.5
$K^+@C_{18}$	-1284.99095	-1284.98457	4.0	866.2
$Rb^+@C_{18}$	-709.23405	-709.22630	4.9	3698.6
$Cs^+@C_{18}$	-705.29734	-705.28929	5.1	5069.4

[a] The difference between G^{in} and G^{out}, $\Delta G = G^{out} - G^{in}$.

[b] $K^{in/out} = \frac{n^{in}}{n^{out}} = e^{(G^{out}-G^{in})/RT}$.

The distances between M^+ and the geometric center of C_{18} ring (d_0), as well as the distances between M^+ and the nearest and farthest C atoms of C_{18} (d_1 and d_2, respectively) are shown in Table 2. Combining Figure 1 as well as Tables S1 and 2, it can be seen that for complexes $M^+@C_{18}^{in}$ with $M^+ = Li^+$, Na^+, K^+, and Rb^+, the metal ions are located on the plane of the C_{18} and gradually approach the geometric center of the ring as the atomic number increases, however, Cs^+ ion, due to the steric hindrance caused by the larger ionic radius, is 0.673 Å vertically offset from geometric center of the C_{18}. No matter which metal ion is complexed with, the deformation of the C_{18} ring does not appear obvious, showcasing a degree of rigidity in its structure.

Table 2 Distances between M^+ from the geometric center of C_{18} (d_0, in Å), distances between M^+ and the nearest and farthest C atoms of C_{18} (d_1 and d_2, in Å), point group (PG), NPA charge of M^+ [$q(M^+)$, in e], and the max Wiberg bond order of $M^+\cdots C$

[$BO(M^+\cdots C)^{max}$] in $M^+@C_{18}^{in}$

	d_0	d_1	d_2	Δd^a	PG	$q(M^+)$	$BO(M^+\cdots C)^{max}$
$Li^+@C_{18}^{in}$	1.647	2.240	5.437	3.197	C_s	0.980	0.098
$Na^+@C_{18}^{in}$	1.026	2.818	4.835	2.017	C_s	0.987	0.112
$K^+@C_{18}^{in}$	0.005	3.689	3.698	0.009	D_{9h}	0.980	0.045
$Rb^+@C_{18}^{in}$	0.004	3.690	3.698	0.008	D_{9h}	0.985	0.055
$Cs^+@C_{18}^{in}$	0.673	3.756	3.758	0.002	C_{9v}	0.984	0.066

[a] The difference between d_1 and d_2, $\Delta d = d_2 - d_1$, in Å.

Some characteristic parameters related to electronic structure, including NPA charge and Wiberg bond order, of $M^+@C_{18}^{in}$ are also listed in Table 2. It can be seen that the positive charge of the $M^+@C_{18}^{in}$ is concentrated mostly on the M^+, while C_{18} ring are essentially in a neutral state. The experimental studies on the structure and optical properties of $Li^+@C_{60}^{in}$ also obtained the conclusion that C_{60} is almost electrically neutral,[60] which confirms the electron-accepting feature of C_{18} ring similar to C_{60}, because even when combined with cations, they can still keep their electrons from losing. The fairly small Wiberg bond order between M^+ and C atoms in C_{18} moiety [$BO(M^+\cdots C)^{max}$] reveals that the contribution of electron-sharing effect to $M^+\cdots C_{18}$ binding can be neglected.

3.2 Binding Interaction in $M^+@C_{18}^{in}$

The independent gradient model based on Hirshfeld partition (IGMH) is a popular method in graphically displaying occurrence region and nature of non-covalent interactions.[61] It can be seen form Figure 2 that the main interaction region in $M^+@C_{18}^{in}$ becomes wider as atomic radius increases in the order of Li^+–Na^+–K^+. In sharp contrast, K^+, Rb^+, and Cs^+ interact equally with all C atoms in C_{18} as shown by the perfect circular δg^{inter} isosurfaces and consistent atomic coloring in the IGMH maps, because they have sufficiently large radii. Furthermore, all IGMH isosurfaces are basically green, indicating very low electron density in the interaction region of M^+ and C_{18}; this again demonstrates that no evident covalent interaction is

formed between M^+ and C_{18}, as covalent interaction always causes notable electron concentration. This observation is also consistent with the Wiberg bond order analysis, and somewhat explains why K^+, Rb^+, and Cs^+ much more tend to be adsorbed inside C_{18} than Li^+ and Na^+, because the former three will interact with significantly fewer C_{18} atoms if they are adsorbed outside.

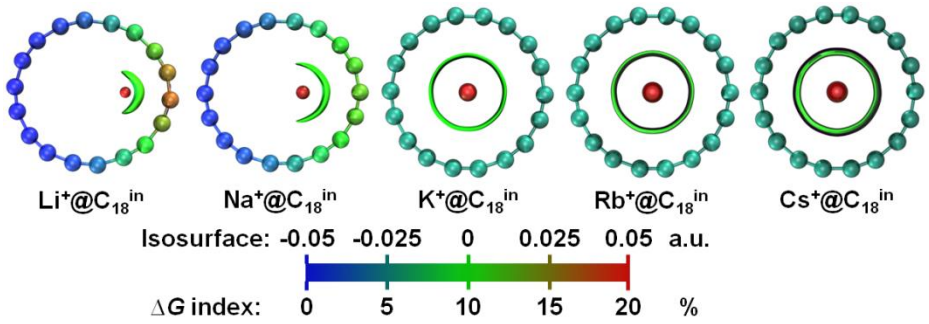

Figure 2. Isosurface map of IGMH of $M^+@C_{18}^{in}$ with δg^{inter} isovalue of 0.001 a.u. Each atom is colored according to its percentage contributions of ΔG index.

In order to study binding strength between M^+ and C_{18} from energetic point of view, we calculated interaction energy (ΔE_{int}), binding energy (ΔE_{bind}), and binding free energy (ΔG_{bind}) of $M^+@C_{18}^{in}$ at gas standard state (298.15 K and 1 atm). Three types of energy defined as $\Delta E_{int} = E(M^+@C_{18}^{in}) - [E(M^+) + E(C_{18}^{complex})]$, $\Delta E_{bind} = E(M^+@C_{18}^{in}) - [E(M^+) + E(C_{18}^{free})]$, and $\Delta G_{bind} = G(M^+@C_{18}^{in}) - [G(M^+) + G(C_{18}^{free})]$, where $C_{18}^{complex}$ and C_{18}^{free} refer to C_{18} in complexed and free-state structures, respectively. It can be seen from Table S3 that Li^+ has strongest binding strength with C_{18} ring, followed by Na^+ and then K^+, while there is no evident difference in binding strength among K^+, Rb^+, and Cs^+, which is in line with the observation of the isosurfaces in IGMH map. From the physical sense, ΔE_{int} and ΔE_{bind} differ by deformation energy (ΔE_{def}) of C_{18} during the complexation. It was found that complexation of C_{18} with Li^+ and Na^+ leads to ΔE_{def} of 1.4 and 0.6 kcal/mol, respectively, while ΔE_{def} is completely negligible in the case of binding to K^+, Rb^+, and Cs^+. The magnitude of ΔE_{def} is closely related to the extent of structural

deformation of C_{18} from its free state (circular shape) to complexed state, and this can be easily recognized from the structure maps in Figure 2. According to the principle of thermodynamics, ΔG_{bind} is the most straightforward metric for determining binding capacity. The ΔG_{bind} data are all distinctly negative, indicating that all M^+ are able to stably bind to C_{18} at least under gas standard state, although penalty effect due to decrease in entropy evidently hinders the complexation to some extent, which is largely exhibited by the clear difference between ΔE_{bind} and ΔG_{bind}.

We also conducted calculation and decomposition of interaction energy at the SAPT2+(3)δMP2 level, which is arranged in Table S4. The interaction energies of complexes $M^+@C_{18}^{in}$ obtained by DFT and SAPT are reasonably consistent, and their change trends with metal atomic numbers are exactly the same, thus confirming their reliability. The energy components extracted from SAPT2+(3)δMP2 calculations for exploring the nature of interaction between M^+ and C_{18} are plotted in Figure 3. It is seen that only the exchange-repulsion that essentially characterizes the steric effect contributes negatively to the binding, while all other components, including electrostatics, induction, and dispersion, promote formation of the complexation to different extents. Comparing different types of metal-doping, it is found that as the atomic number of M^+ increases, dispersion and induction effects between M^+ and C_{18} significantly increase and decrease, respectively, while electrostatics effect does not vary evidently and always contribute little to the complexation. Impressively, the induction effect mainly charactering polarization effect dominates the attractive part of the $M^+\cdots C_{18}$ interaction energy, and for the case of Li^+-doping, it even contributes more than 93%. Although dispersion effect is not as important as induction effect for the studied interactions, its role should never be ignored, especially for M^+ with large atomic numbers. For example, contribution of dispersion effect to $Cs^+\cdots C_{18}$ binding is even comparable to that of induction effect.

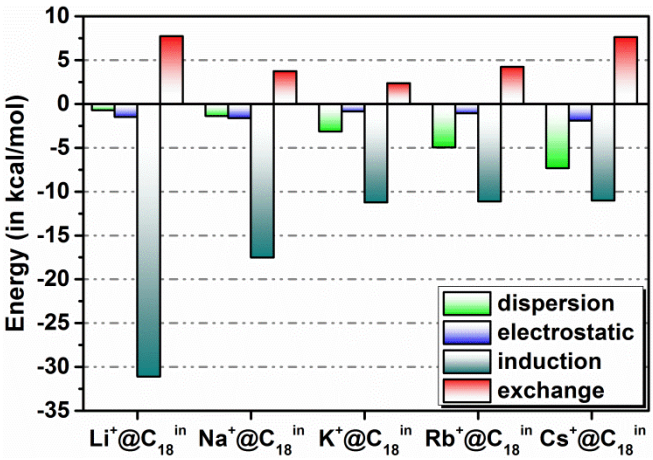

Figure 3. Components of interaction energy between M^+ and C_{18} in $M^+@C_{18}^{in}$ obtained from SAPT2+(3)δMP2 calculations.

3.3 Electronic absorption spectrum of $M^+@C_{18}^{in}$

Electronic absorption spectrum is a conventional but important technique for material analysis, which essentially involves the optical excitation of electrons in molecules. The data related to vertical excitation of $M^+@C_{18}^{in}$ determined by TD-DFT calculations are shown in Tables S5 and S6. The corresponding TD-DFT results are employed to simulate the absorption spectra of the complexes, as shown in Figure 4. The $M^+@C_{18}^{in}$ exhibit characteristic absorption in the wavelength range of about 170 nm to 260 nm, consisting of a super strong peak at 219 nm followed by an extremely weak absorption at 191 nm. It is obvious that M^+ doped C_{18} not only have virtually identical electronic absorption spectra with each other, but their absorption characteristics are also not distinguishably different from that of pristine C_{18},[29] that is to say, the electronic absorption spectra of the complexes $M^+@C_{18}^{in}$ are almost independent of the species or even the existence of the M^+. This observation can be rationalized by the results of NPA charge analysis described above that there is not much charge transfer between M^+ and C_{18} as well as charge transfer spectrum (CTS) depicted below that the electronic absorption spectra of $M^+@C_{18}^{in}$ are almost entirely contributed by the C_{18} moiety. So obviously, the $M^+@C_{18}^{in}$ should still look colorless, just like the pristine C_{18}.

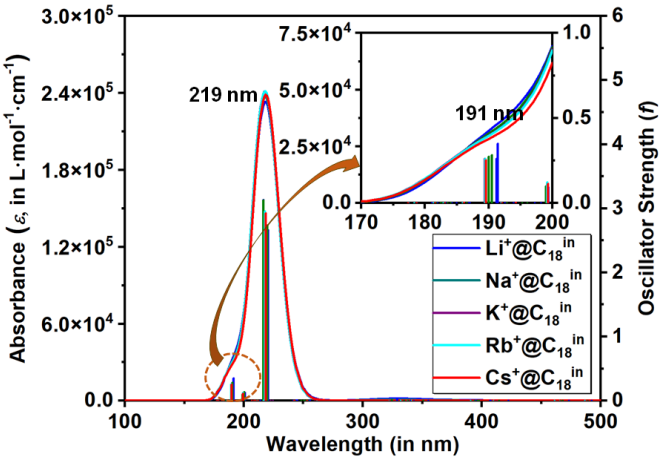

Figure 4. Electronic absorption spectra (curves) and oscillator strengths (spikes) of $M^+@C_{18}^{in}$. The Gaussian function with full width at half-maximum of 0.333 eV was employed for broadening the theoretical data as spectrum curves.

The concept of charge-transfer spectrum (CTS) proposed by us is helpful to understand the nature of electron excitation from the perspective of the contribution of electronic transitions within and between fragments to entirety.[32] By using this approach, the contributions of electron rearrangement and charge transfer to the absorption spectra of $M^+@C_{18}^{in}$ are evaluated and plotted in Figure S1(a)-(e). As can be seen, almost the entire optical absorption of the $M^+@C_{18}^{in}$ is assigned to be an electron excitation within C_{18} moiety, as the red curves representing the electron redistribution in C_{18} ring is extremely similar to the absorption spectrum of the complexes shown in Figure 4. This is precisely why the electronic absorption spectra of $M^+@C_{18}^{in}$ are independent of the metal ion they contain. Furthermore, the electron transfers of $M^+ \rightarrow C_{18}$ and $M^+ \leftarrow C_{18}$ contribute to the same and negligible remaining portion of the electronic absorption spectrum of $M^+@C_{18}^{in}$.

As shown as an example in Figure 5, the maximum absorptions of $Li^+@C_{18}^{in}$ originated from the degenerate electron excitation of $S_0 \rightarrow S_{25}$ and $S_0 \rightarrow S_{26}$ involve many MOs, and there is no specific orbital pair plays a dominate role. Other alkali-metal ions endohedral complexes also exhibit the same excitation characteristics, making it difficult to describe the electron excitation by means of MO picture. In this case, the hole-electron analysis method developed by us can more

conveniently provide the characteristics of electron transitions.[29] The isosurface maps of hole and electron distributions for the excited states involved in maximum absorption of $M^+@C_{18}^{in}$ are given in Figure 6. It can be found that both in-plane and out-of-plane π MOs participate in the excitations since the isosurfaces of holes and electrons involved are distributed around the C-C bonds in the form of circular ring. A more detailed observation reveals that all relevant excitations are electron transfer transitions almost exclusively from short C-C bonds to long C-C bonds. Note that the hole and electron characters of the two degenerate excitations are very similar but different in distribution orientation. The electron excitation characteristics of the complexes $M^+@C_{18}^{in}$ obtained by hole-electron analysis confirm the conclusion of CTS and are very much like the related features of C_{18}.[29]

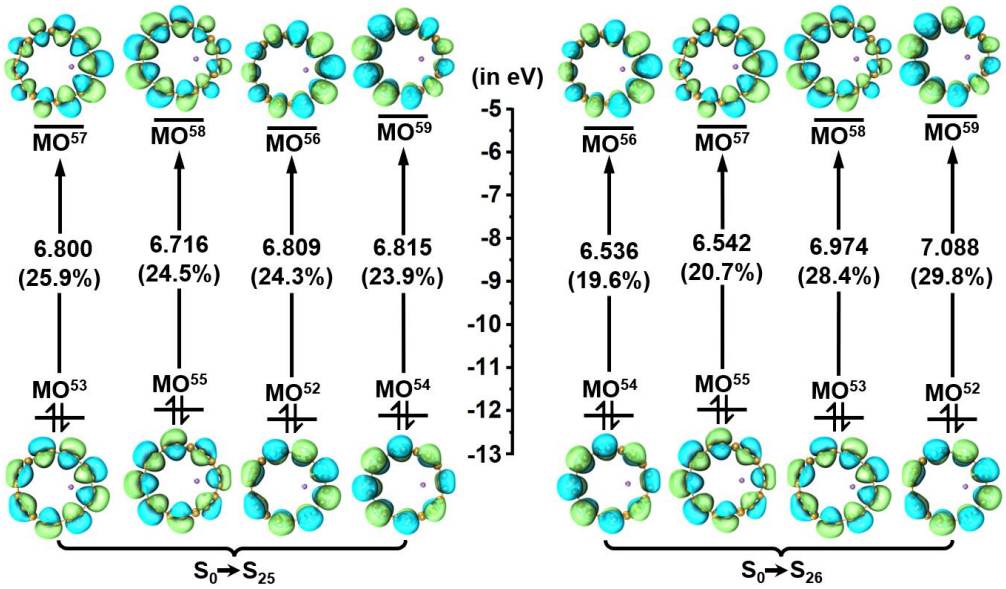

Figure 5. Dominant contributions of MO transitions to (a) $S_0 \rightarrow S_{25}$ and (b) $S_0 \rightarrow S_{26}$ excitations in $Li^+@C_{18}^{in}$ (isovalue = 0.02). Green and blue regions denote the positive and negative orbital phases, respectively. The numbers outside and inside the parentheses denote the energy gaps of orbital and the contributions of the transition to corresponding excitation, respectively.

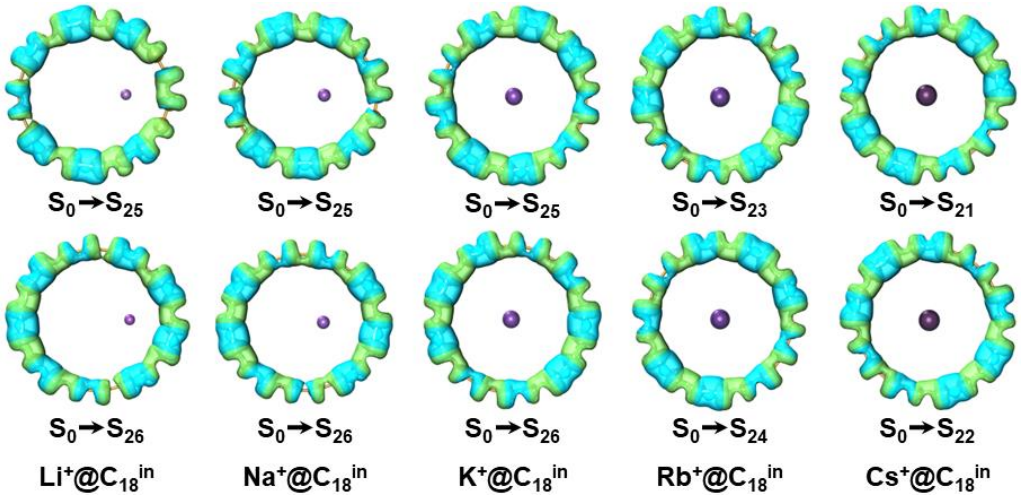

Figure 6. Real space representation of hole and electron distributions for critical excitations related to maximum absorption of $M^+@C_{18}^{in}$ (isovalue = 0.002 a.u.). Green and blue regions denote the hole and electron distributions, respectively.

3.4 Molecular (Hyper)polarizability of $M^+@C_{18}^{in}$

(Hyper)polarizabilities are response properties of a molecule to an external electric field. The (hyper)polarizabilities of $M^+@C_{18}^{in}$ in zero-frequency limit ($\lambda = \infty$ nm) and under frequency-dependent fields (λ = 1907, 1460, 1340, 1180, and 1064 nm) calculated by the coupled perturbed Kohn-Sham (CPKS) method[62] are numerically listed in Table S7. The isotropic average polarizability [$\alpha_{iso}(\lambda)$], the projection of first hyperpolarizability on molecular dipole [$\beta_{vec}(\lambda)$], and the average of second hyperpolarizability [$\gamma_{\|}(\lambda)$] in zero-frequency limit ($\lambda = \infty$ nm) are shown in Figure 7, and their analogues under frequency-dependent fields (λ = 1907, 1460, 1340, 1180, and 1064 nm), which can be directly compared with experimental observations, are illustrated in Figure 8, respectively.

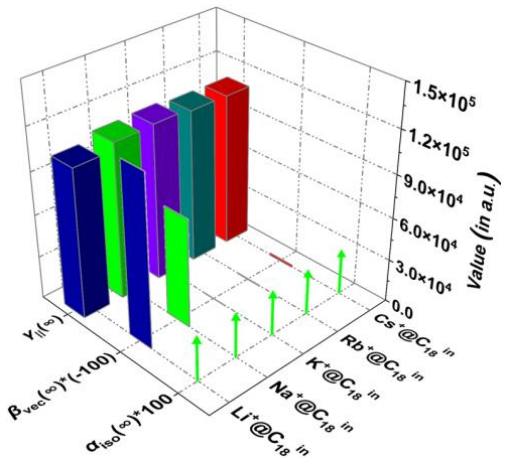

Figure 7. Calculated molecular (hyper)polarizability of $M^+@C_{18}^{in}$ in zero-frequency limit.

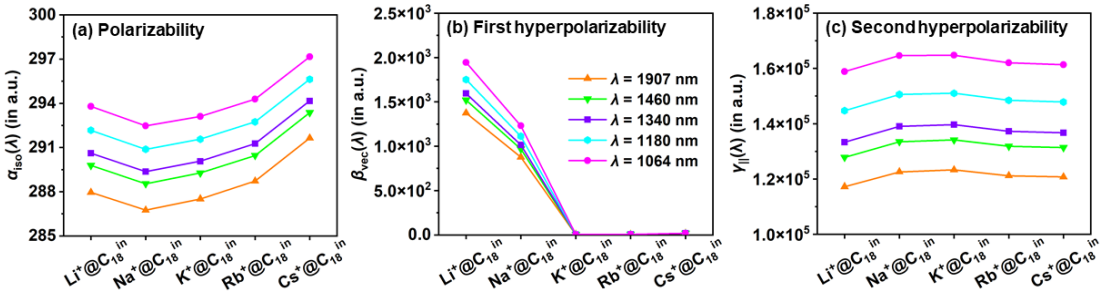

Figure 8. Calculated molecular (hyper)polarizability of $M^+@C_{18}^{in}$ under electric field of different frequency: (a) the isotropic average polarizability [$\alpha_{iso}(\lambda)$], (b) the projection of first hyperpolarizability on molecular dipole [$\beta_{vec}(\lambda)$], and (c) the average of second hyperpolarizability [$\gamma_{||}(\lambda)$].

Under the action of incident light with specific frequency, there is almost no distinction in $\alpha_{iso}(\lambda)$ of different $M^+@C_{18}^{in}$, and the variation of $\gamma_{||}(\lambda)$ with the complexed metal ion is also subtle. This is because the charges of all M^+ are close to +1 *e*, so the polarizabilities of them are small, and the polarization properties of C_{18} unit are similar due to its electronic structure is almost unaffected by complextion. Taken together, the $\alpha_{iso}(\lambda)$ and $\gamma_{||}(\lambda)$ of $M^+@C_{18}^{in}$ with different metal ions do not differ significantly under certain frequencies of incident light. The components of (hyper)polarizability tensor parallel to the plane of ring (i.e., *xy* plane), $\alpha_{xx}(\lambda)$ and $\alpha_{yy}(\lambda)$ as well as $\gamma_{xxxx}(\lambda)$ and $\gamma_{yyyy}(\lambda)$, are obviously larger than those perpendicular to the ring, i.e., $\alpha_{zz}(\lambda)$ and $\gamma_{zzzz}(\lambda)$. Moreover, the components of $\alpha_{iso}(\lambda)$ and $\gamma_{||}(\lambda)$ in the long axis

(i.e., *x* axis) of $M^+@C_{18}^{in}$ with M^+ = Li^+ and Na^+ that deviate from the nine-fold symmetry are slightly higher than those in their short axis (i.e., *y* axis), while the two axial components of $M^+@C_{18}^{in}$ with M^+ = K^+, Rb^+, and Cs^+ are almost equal. These observations are due to the fact that π electrons in C_{18} have a wider delocalization space parallel to the ring plane, and it is more prominent in the long axis direction.

As for the case of $\beta_{vec}(\lambda)$, the $M^+@C_{18}^{in}$ with different metal ions exhibits different behavior, wherein $Li^+@C_{18}^{in}$ has the highest value, $Na^+@C_{18}^{in}$ has a smaller value, $K^+@C_{18}^{in}$ and $Rb^+@C_{18}^{in}$ have a value almost zero, and $Cs^+@C_{18}^{in}$ has a very small value. Obviously, the $\beta_{vec}(\lambda)$ of these complexes is closely related to their molecular symmetry, that is, the larger the molecular deviation from the centrosymmetric structure, the greater the $\beta_{vec}(\lambda)$ value. The component of $\beta_{vec}(\lambda)$ in the long axis of $M^+@C_{18}^{in}$ with M^+ = Li^+ and Na^+ dominates the contribution to the total first hyperpolarizability, while the components in the molecular plane of $M^+@C_{18}^{in}$ with M^+ = K^+ and Rb^+ is essentially zero due to the approximate centrosymmetric structure. Strictly planar structure makes the components of the $\beta_{vec}(\lambda)$ of $M^+@C_{18}^{in}$ (M^+ = Li^+, Na^+, K^+, and Rb^+) in the *z* direction zero, while in contrast, the small $\beta_{vec}(\lambda)$ of $Cs^+@C_{18}^{in}$ is mainly contributed by its *z*-component, as Cs^+ is located vertically outside the ring. It can be seen that different alkali-metal ions, due to their different radii and properties, can composite with C_{18} to regulate the first hyperpolarizability of the system.

The frequency-dependent (hyper)polarizabilities $\alpha_{iso}(\lambda)$, $\beta_{vec}(\lambda)$, and $\gamma_{||}(\lambda)$ (λ = 1907, 1460, 1340, 1180, and 1064 nm) are substantially higher than those in the zero-frequency limit ($\lambda = \infty$ nm) for all complexes $M^+@C_{18}^{in}$ and the resonance effect of the (hyper)polarizability induced by incident light amplifies steadily with the light frequency.

The above observations indicate that Li^+-doped complex exhibits the most prominent nonlinear optical (NLO) properties. Therefore, the following in-depth analysis of the (hyper)polarizabilities of $M^+@C_{18}^{in}$ will be conducted using $Li^+@C_{18}^{in}$ in zero-frequency limit as an example.

(Hyper)polarizability density is a very useful manner to visually exhibit

contribution of different regions to molecular (hyper)polarizability.[29,32,37,63-66] It can be seen from the (hyper)polarizability density for $Li^+@C_{18}^{in}$ in Figure 9 that for $i = x$ and y, the $-i\rho_i^{(1)}(\vec{r})$ and $-i\rho_{iii}^{(3)}(\vec{r})$ functions exhibit impressive large positive isosurfaces at both ends of the carbon ring, which reasonably explains the fact that the polarizabilities and second hyperpolarizabilities of the complex have large components in these directions. In contrast, the density distribution of the $-i\rho_{ii}^{(2)}(\vec{r})$ prevents us from visually quantifying the magnitude of the first hyperpolarizability component of $Li^+@C_{18}^{in}$. With the isovalues setted in Figure 8, the isosurfaces of (hyper)polarizability density corresponding to $i = z$ do not occur due to the very small function values, which is in line with the fact that the z components of (hyper)polarizability are much smaller than x and y components. Taken overall, the isosurface is invisible over Li^+, which means that the contribution of Li^+ to the (hyper)polarizability is negligible, as expected, because Li^+ has no valence electrons and its core electrons have little response to external fields.

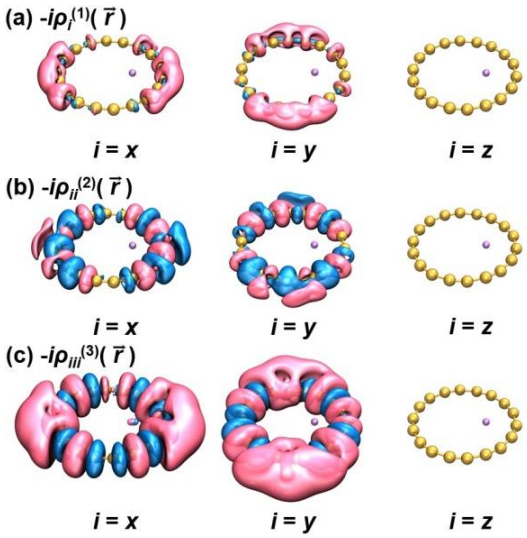

Figure 9. Plots of local contribution of (hyper)polarizability densities of $Li^+@C_{18}^{in}$ in zero-frequency limit: (a) $-i\rho_i^{(1)}(\vec{r})$ for the polarizability (isovalue = 0.6 a.u.), (b) $-i\rho_{ii}^{(2)}(\vec{r})$ for the first hyperpolarizability (isovalue = 6.0 a.u.),

and (c) $-i\rho_{iii}^{(3)}(\vec{r})$ for the second hyperpolarizability (isovalue = 60.0 a.u.). Pink and blue regions denote positive and negative contributions, respectively.

In order to visually display the interesting anisotropic character of the molecular (hyper)polarizability rom different perspectives, the unit sphere representation map of (hyper)polarizability tensor of $Li^+@C_{18}^{in}$ is plotted and shown in Figure 10.[67] The anisotropy of the (hyper)polarizability of $Li^+@C_{18}^{in}$ is clearly visible from the tensor maps, and the hyperpolarizability tensors parallel to the ring plane is significantly stronger than that of the perpendicular one. More specifically, for polarizability and second hyperpolarizability, the tensors in all directions along the ring plane are identical, while the tensors of first hyperpolarizability clearly follows the negative *x*-axis direction. The characteristics of molecular (hyper)polarizability tensors are consistent with the values of the (hyper)polarizability components analysis above.

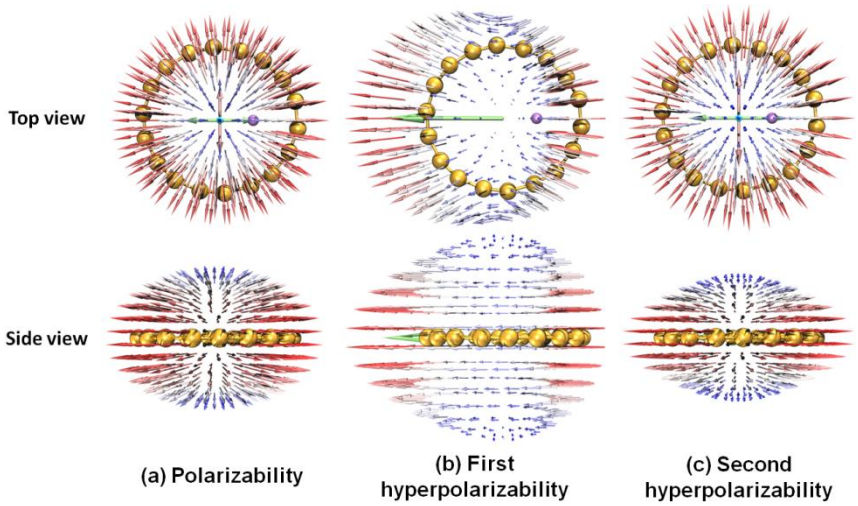

Figure 10. Unit sphere representation of (a) the polarizability tensor, (b) the first hyperpolarizability tensor, and (c) the second hyperpolarizability tensor of $Li^+@C_{18}^{in}$ in zero-frequency limit. The length and the color of the arrows represent magnitude of (hyper)polarizability in different directions.

4. Conclusions

The geometric and electronic structures, binding interactions, electronic absorption

spectra, and (hyper)polarizabilities of designed complexes $M^+@C_{18}^{in}$ by M^+ endohedral C_{18} were studied by using (TD-)DFT method in this work. Due to the difference in radius, different M^+ ions complex with C_{18} at different positions in the ring. The binding interaction is found to be strongest for $Li^+@C_{18}^{in}$ among the $M^+@C_{18}^{in}$ with different alkali-metal ions. Atomic charge analysis shows that all M^+ in the complexes carry charge of almost +1.0 *e*, while the C_{18} moiety basically keeps neutral like its pristine status. The nature of the complexation mainly comes from induction term and/or the dispersion term, depending on the type of M^+. Theoretical electronic spectra show that all complexes have the same optical absorption characteristics as the pristine C_{18}, mainly because the electronic excitation of the complexes contributed almost solely by the redistribution of electrons within the C_{18} ring, which is demonstrated by both CTS and hole-electron analyses. Furthermore, it is found that the electron transition within C_{18} is exclusively from short C-C bonds to long C-C bonds. The studies of the NLO properties of the external field response of the $M^+@C_{18}^{in}$ indicate that, under the action of incident light with specific frequency, there is no significant distinction in molecular polarizability and second hyperpolarizability of complexes with difference M^+, while the first hyperpolarizability can be regulated by the species of doped alkali-metal ions. For all complexes $M^+@C_{18}^{in}$, the frequency-dependent (hyper)polarizabilities are substantially higher than those in the zero-frequency limit, and the higher the incident frequency, the greater the molecular (hyper)polarizability, indicating obvious resonance effect of the external field on molecular optical nonlinearity. Moreover, the analyses of the (hyper)polarizability densities and (hyper)polarizability tensors of the complexes reveal in depth the inherent characteristics of their optical nonlinearity.

Cyclocarbons are a type of system that have recently come into the view of chemists and may have great application potential in the future. We believe this work can provide guidance for experimental research on the application of cyclocarbons in alkali-metal ion storage and the possibility of process complexes as optoelectronic functional materials.

Supporting Information

Optimized Cartesian coordinates of $M^+@C_{18}^{in}$ and $M^+@C_{18}^{out}$; interaction energy, binding energy, and binding free energy between M^+ and C_{18} of $M^+@C_{18}^{in}$; calculated absorption wavelengths, involved excited states, oscillator strengths, transition energies, and main transition orbitals for $M^+@C_{18}^{in}$ at about 219 and 191 nm; charge-transfer spectrum of $M^+@C_{18}^{in}$; (hyper)polarizabilities of $M^+@C_{18}^{in}$ in zero-frequency limit and under frequency-dependent field (PDF)

Notes

The authors declare no competing financial interest.

Acknowledgements

This work was supported by the Postgraduate Research & Practice Innovation Program of Jiangsu Province (SJCX23_2158).

References

(1) Pan, Q.; Wu, Y.; Zhong, W.; Zheng, F.; Li, Y.; Liu, Y.; Hu, J.; Yang, C. Carbon Nanosheets Encapsulated NiSb Nanoparticles as Advanced Anode Materials for Lithium-Ion Batteries. Energy Environ. Mater. 2020, 3, 186−191.

(2) Zhao, C.; Wang, Q.; Yao, Z.; Wang, J.; Sánchez-Lengeling, B.; Ding, F.; Qi, X.; Lu, Y.; Bai, X.; Li, B.; Li, H.; Aspuru-Guzik, A.; Huang, X.; Delmas, C.; Wagemaker, M.; Chen, L.; Hu, Y.-S. Rational Design of Layered Oxide Materials for Sodium-Ion Batteries. Science 2020, 370, 708−711.

(3) Shen, X.; Zhou, Q.; Han, M.; Qi, X.; Li, B.; Zhang, Q.; Zhao, J.; Yang, C.; Liu, H.; Hu, Y.-S. Rapid Mechanochemical Synthesis of Polyanionic Cathode with Improved Electrochemical Performance for Na-Ion Batteries. Nat. Commun. 2021, 12, 2848.

(4) Wang, L.; Lu, Y.; Liu, J.; Xu, M.; Cheng, J.; Zhang, D.; Goodenough, J. B. A Superior Low-Cost Cathode for a Na-Ion Battery. Angew. Chem., Int. Ed. 2013, 125, 2018−2021.

(5) Bai, P.; He, Y.; Xiong, P.; Zhao, X.; Xu, K.; Xu, Y. Long cycle life and High Rate Sodium-Ion

Chemistry for Hard Carbon Anodes. Energy Storage Mater. 2018, 13, 274−282.

(6) Luo, W.; Wan, J.; Ozdemir, B.; Bao, W.; Chen, Y.; Dai, J.; Lin, H.; Xu, Y.; Gu, F.; Barone, V.; Hu, L. Potassium Ion Batteries with Graphitic Materials. Nano Lett. 2015, 15, 7671−7677.

(7) Li, B.; Zhao, J.; Zhang, Z.; Zhao, C.; Sun, P.; Bai, P.; Yang, J.; Zhou, Z.; Xu, Y. Electrolyte-Regulated Solid-Electrolyte Interphase Enables Long Cycle Life Performance in Organic Cathodes for Potassium-Ion Batteries. Adv. Funct. Mater. 2018, 29, 1807137.

(8) Kothandam, G.; Singh, G.; Guan, X.; Lee, J. M.; Ramadass, K.; Joseph, S.; Benzigar, M.; Karakoti, A.; Yi, J.; Kumar, P.; Vinu A. Recent Advances in Carbon-Based Electrodes for Energy Storage and Conversion. Adv. Sci. 2023, 10, 2301045, and references therein.

(9) F. Diederich, Y. Rubin, C. B. Knobler, R. L. Whetten, K. E. Schriver, K. N. Houk, Y. I. Li, All-carbon molecules: Evidence for the generation of cyclo[18]carbon from a stable organic precursor, Science 1989, 245, 1088–1090.

(10) S. W. McElvany, M. M. Ross, N. S. Goroff, F. Diederich, Cyclocarbon coalescence: Mechanisms for tailor-made fullerene formation, Science 1993, 259, 1594–1596.

(11) G. von Helden, N. G. Gotts, M. T. Bowers, Experimental evidence for the formation of fullerenes by collisional heating of carbon rings in the gas phase, Nature 1993, 363, 60–63.

(12) F. Diederich, Carbon scaffolding: Building acetylenic all-carbon and carbon-rich compounds, Nature 1994, 369, 199–207.

(13) Kaiser, K.; Scriven, L. M.; Schulz, F.; Gawel, P.; Gross, L.; Anderson, H. L. An sp-hybridized molecular carbon allotrope, cyclo[18]carbon. Science 2019, 365, 1299–1301.

(14) Baryshnikov, G. V.; Valiev, R. R.; Kuklin, A. V.; Sundholm, D.; Ågren, H. Cyclo[18]carbon: Insight into Electronic Structure, Aromaticity and Surface Coupling. J. Phys. Chem. Lett. 2019, 10, 6701–6705.

(15) Fang, S.; Hu, Y. Cyclo[18]carbon as an Ultra-Elastic Molecular O-Ring with Unique Mechanical Properties. Carbon 2021, 171, 96–103.

(16) Raeber, A. E.; Mazziotti, D. A. Non-Equilibrium Steady State Conductivity in Cyclo[18]carbon and Its Boron Nitride Analogue. Phys. Chem. Chem. Phys. 2020, 22, 23998–24003.

(17) Zhang, L.; Li, H.; Feng, Y.; Shen, L. Diverse Transport Behaviors in Cyclo[18]carbon-Based Molecular Devices. J. Phys. Chem. Lett. 2020, 11, 2611–2617.

(18) Stasyuk, A. J.; Stasyuk, O. A.; Solà, M.; Voityuk, A. A. Cyclo[18]carbon: The Smallest All-Carbon Electron Acceptor. Chem. Commun. 2020, 56, 352−355.

(19) Dai, C.; Chen, D.; Zhu, J. Achieving Adaptive Aromaticity in Cyclo[10]carbon by Screening Cyclo[*n*]carbon (*n* = 8–24). Chem. Asian. J. 2020, 15, 2187–2191.

(20) Pereira, Z. S.; da Silva, E. Z. Spontaneous Symmetry Breaking in Cyclo[18]carbon. J. Phys. Chem. A 2020, 124, 1152−1157.

(21) Fang, S.; Hu, Y. H. Creating and Seeing the First Pure Carbon Ring. Matter 2019, 1, 1116–1118.

(22) Fedik, N.; Kulichenko, M.; Steglenko, D. Can Aromaticity be a Kinetic Trap? Example of Mechanically Interlocked Aromatic [2-5]Catenanes Built from Cyclo[18]carbon. Chem. Commun. 2020, 56, 2711−2714.

(23) Hussain, S.; Chen, H.; Zhang, Z.; Zheng, H. Vibrational Spectra and Chemical Imaging of Cyclo[18]carbon by Tip Enhanced Raman Spectroscopy. Chem. Commun. 2020, 56, 2336–2339.

(24) Chen, J.; Sun, L.; Zhang, R. Reaction Mechanisms of Cyclo[18]carbon and Triplet Oxygen. Phys. Chem. Chem. Phys. 2021, 23, 17545–17552.

(25) Chen, J.; Zhang, R. Strong Interaction between Cyclo[18]carbon and Grapheme. Adv. Theory Simul. 2021, 4, 2100022.

(26) Jiang, Y.; Mattioli, E. J.; Calvaresi, M.; Wang, Z. Theoretical Design of an Ultrafast Supramolecular Rotor Composed of Carbon Nano-Rings. Chem. Commun. 2020, 56, 11835–11838.

(27) Suresh, R.; Baryshnikov, G. V.; Kuklin, A. V.; Nemkova, D. I.; Saikova, S. V.; Ågren, H. Cyclo[18]carbon Formation from $C_{18}Br_6$ and $C_{18}(CO)_6$ Precursors. J. Phys. Chem. Lett. 2022, 13, 10318–10325.

(28) Zhang, L.; Li, H.; Feng, Y. P.; Shen, L. Diverse Transport Behaviors in Cyclo[18]carbon-Based Molecular Devices. J. Phys. Chem. Lett. 2020, 11, 2611–2617.

(29) Liu, Z.; Lu, T.; Chen, Q. An Sp-Hybridized All-Carboatomic Ring, Cyclo[18]carbon: Electronic Structure, Electronic Spectrum, and Optical Nonlinearity. Carbon 2020, 165, 461–467.

(30) Liu, Z.; Lu, T.; Chen, Q. An Sp-Hybridized All-Carboatomic Ring, Cyclo[18]carbon: Bonding Character, Electron Delocalization, and Aromaticity. Carbon 2020, 165, 468–475.

(31) Liu, Z.; Lu, T.; Chen, Q. Intermolecular Interaction Characteristics of the All-Carboatomic

Ring, Cyclo[18]carbon: Focusing on Molecular Adsorption and Stacking. Carbon 2021, 171, 514–523.

(32) Liu, Z.; Wang, X.; Lu, T.; Yuan, A.; Yan, X. Potential Optical Molecular Switch: Lithium@cyclo[18]carbon Complex Transforming between Two Stable Configurations. Carbon 2022, 187, 78–85.

(33) Liu, Z.; Wang, X.; Lu, T.;Yan, X.;Wang, J.;Wu, Y.;Xu, J.;Xie,Z. Theoretical Design of a Dual-Motor Nanorotator Composed of All-Carboatomic Cyclo[18]carbon and Figure-of-Eight Carbon Hoop. Chem. Commun. 2023, 59, 9770–9773.

(34) Yang Wu, Zeyu Liu, Tian Lu, Mesías Orozco-Ic, Jingbo Xu, Xiufen Yan, Jiaojiao Wang, Xia Wang, Exploring the Aromaticity Differences of Isoelectronic Species of Cyclo[18]carbon (C_{18}), $B_6C_6N_6$ and B_9N_9: The Role of Carbon Atoms as Connecting Bridges. Inorg. Chem. 2023, 62, 19986–19996.

(35) Wang, X.; Liu, Z.; Yan, X.; Lu, T.; Zheng, W.; Xiong, W. Bonding Character, Electron Delocalization, and Aromaticity of Cyclo[18]carbon (C_{18}) Precursors, C_{18}-$(CO)_n$ (n = 6, 4, and 2): Focusing on the Effect of Carbonyl (-CO) Groups. Chem. Eur. J. 2022, 28, e202103815.

(36) Wang, X.; Liu, Z.; Wang, J.; Lu, T.; Xiong, W.; Yan, X.; Zhao, M. Orozco-Ic, M., Electronic Structure and Aromaticity of an Unusual Cyclo[18]carbon Precursor, $C_{18}Br_6$. Chem. Eur. J. 2023, 29, e202300348.

(37) Wang, X.; Liu, Z.; Yan, X.; Lu, T.; Wang, H.; Xiong, W.; Zhao, M. Photophysical Property and Optical Nonlinearity of Cyclo[18]carbon (C_{18}) Precursors, C_{18}-$(CO)_n$ (n = 2, 4, and 6): Focusing on the Effect of Carbonyl (-CO) Groups. Phys. Chem. Chem. Phys. 2022, 24, 7466–7473.

(38) Liu, Z.; Wang, X.; Lu, T.; Wang, J.; Yan, X.; Wu, Y.; Xu, J. Molecular Assembly with Figure-of-Eight Nanohoop as a Strategy for Collection and Stabilization of Cyclo[18]carbon. Phys. Chem. Chem. Phys. 2023, 25, 16707–16711.

(39) Liu, Z.; Lu, T.; Chen, Q. Vibrational Spectra and Molecular Vibrational Behaviors of All-Carboatomic Rings, Cyclo[18]carbon and Its Analogues. Chem. Asian J. 2021, 16, 56–63.

(40) Liu, Z.; Lu, T.; Yuan, A.; Wang, X.; Chen, Q.; Yan, X. Remarkable Size Effect on Photophysical and Nonlinear Optical Properties of All-Carboatomic Rings, Cyclo[18]carbon and Its Analogues. Chem. Asian. J. 2021, 16, 2267–2271.

(41) Liu, Z.; Lu, T.; Chen, Q. Comment on “Theoretical Investigation on Bond and Spectrum of Cyclo[18]carbon (C_{18}) with Sp-Hybridized”. J. Mol. Model. 2021, 27, 42.

(42) Lu, T.; Chen, Q. Ultrastrong Regulation Effect of the Electric Field on the All-Carboatomic Ring Cyclo[18]carbon. Chem. Phys. Chem. 2021, 22, 386–395.

(43) Lu, T.; Liu, Z.; Chen, Q. Accurate Theoretical Evaluation of Strain Energy of All-Carboatomic Ring (Cyclo[2*n*]carbon), Boron Nitride Ring, and Cyclic Polyacetylene. Chin. Phys. B 2022, 31, 126101.

(44) Lu, T.; Liu, Z.; Chen, Q. Comment on “18 and 12 – Member Carbon Rings (Cyclo[*n*]carbons) – A Density Functional Study”. Mat. Sci. Eng. B 2021, 273, 115425.

(45) Scriven, L. M.; Kaiser, K.; Schulz, F.; Sterling, A. J.; Woltering, S. L.; Gawel, P.; Christensen, K. E.; Anderson, H. L.; Gross, L. Synthesis of Cyclo[18]carbon via Debromination of $C_{18}Br_6$. J. Am. Chem. Soc. 2020, 142, 12921–12924.

(46) Gao, Y.; Albrecht, F.; Rončević, I.; Ettedgui, I.; Kumar, P.; Scriven, L. M.; Christensen, K. E.; Mishra, S.; Righetti, L.; Rossmannek, M.; Tavernelli, I.; Anderson, H. L.; Gross, L. On-Surface Synthesis of a Doubly Anti-Aromatic Carbon Allotrope. Nature 2023, 623, 977–981.

(47) Sun, L.; Zheng, W.; Gao, W.; Kang, F.; Zhao, M.; Xu, W. On-Surface Synthesis of Aromatic Cyclo[10]carbon and Cyclo[14]carbon. Nature 2023, 623, 972–976.

(48) Chai, J.-D.; Head-Gordon, M. Long-Range Corrected Hybrid Density Functionals with Damped Atom–Atom Dispersion Corrections. Phys. Chem. Chem. Phys. 2008, 10, 6615–6620.

(49) Weigend, F.; Ahlrichs, R. Balanced Basis Sets of Split Valence, Triple Zeta Valence and Quadruple Zeta Valence Quality for H to Rn: Design and Assessment of Accuracy. Phys. Chem. Chem. Phys. 2005, 7, 3297–3305.

(50) Zheng, J.; Xu, X.; Truhlar, D.G. Minimally Augmented Karlsruhe Basis Sets. Theor. Chem. Acc. 2011, 128, 295–305.

(51) Mardirossian, N.; Head-Gordon, M. ωB97M-V: A Combinatorially Optimized, Range-Separated Hybrid, Meta-GGA Density Functional with VV10 Nonlocal Correlation. J. Chem. Phys. 2016, 144, 214110.

(52) Weigend, F.; Ahlrichs, R. Balanced Basis Sets of Split Valence, Triple Zeta Valence and Quadruple Zeta Valence Quality for H to Rn: Design and Assessment of Accuracy. Phys. Chem. Chem. Phys. 2005, 7, 3297–3305.

(53) Prascher, B. P.; Woon, D. E.; Peterson, K. A.; Dunning, T. H.; Wilson, A. K. Gaussian Basis Sets for Use in Correlated Molecular Calculations. VII. Valence, Core-Valence, and Scalar Relativistic Basis Sets for Li, Be, Na, and Mg. Theor. Chem. Acc. 2011, 128, 69–82.

(54) Hill, J. G.; Peterson, K. A. Gaussian Basis Sets for Use in Correlated Molecular Calculations. XI. Pseudopotential-Based and All-Electron Relativistic Basis Sets for Alkali Metal (K-Fr) and Alkaline Earth (Ca-Ra) Elements. J Chem. Phys. 2017, 147, 244106.

(55) Frisch, M. J.; Trucks, G. W.; Schlegel, H. B.; Scuseria, G. E.; Robb, M. A.; Cheeseman, J. R.; Scalmani, G.; Barone, V.; Petersson, G. A.; Nakatsuji, H.; Li, X.; Caricato, M.; Marenich, A. V.; Bloino, J.; Janesko, B. G.; Gomperts, R.; Mennucci, B.; Hratchian, H. P.; Ortiz, J. V.; Izmaylov, A. F.; Sonnenberg, J. L.; Williams; Ding, F.; Lipparini, F.; Egidi, F.; Goings, J.; Peng, B.; Petrone, A.; Henderson, T.; Ranasinghe, D.; Zakrzewski, V. G.; Gao, J.; Rega, N.; Zheng, G.; Liang, W.; Hada, M.; Ehara, M.; Toyota, K.; Fukuda, R.; Hasegawa, J.; Ishida, M.; Nakajima, T.; Honda, Y.; Kitao, O.; Nakai, H.; Vreven, T.; Throssell, K.; Montgomery Jr., J. A.; Peralta, J. E.; Ogliaro, F.; Bearpark, M. J.; Heyd, J. J.; Brothers, E. N.; Kudin, K. N.; Staroverov, V. N.; Keith, T. A.; Kobayashi, R.; Normand, J.; Raghavachari, K.; Rendell, A. P.; Burant, J. C.; Iyengar, S. S.; Tomasi, J.; Cossi, M.; Millam, J. M.; Klene, M.; Adamo, C.; Cammi, R.; Ochterski, J. W.; Martin, R. L.; Morokuma, K.; Farkas, O.; Foresman, J. B.; Fox, D. J. Gaussian 16 Rev. A.03, 2016.

(56) Neese, F. Software update: the ORCA program system, version 4.0, WIREs Comput. Mol. Sci. 2018, 8, e1327.

(57) Parrish, R. M.; Burns, L. A.; Smith, D. G. A.; Simmonett, A. C.; DePrince, A. E.; Hohenstein, E. G.; Bozkaya, U.; Sokolov, A. Y.; Remigio, R. D.; Richard, R. M.; Gonthier, J. F.; James, A. M.; McAlexander, H. R.; Kumar, A; Saitow, M.; Wang, X.; Pritchard, B. P.; Verma, P.; Schaefer, III H. F.; Patkowski, K.; King, R. A.; Valeev, E. F.; Evangelista F. A.; Turney, J. M.; Daniel Crawford, T.; Sherrill, C. D. Psi4 1.1: An Open-Source Electronic Structure Program Emphasizing Automation, Advanced Libraries, and Interoperability. J. Chem. Theory. Comput. 2017, 13, 3185–3197.

(58) Lu, T.; Chen, F. Multiwfn: A Multifunctional Wavefunction Analyzer. J. Comput. Chem. 2012, 33, 580–592.

(59) Humphrey, W.; Dalke, A.; Schulten, K. VMD: Visual Molecular Dynamics. J. Mol. Graph. 1996, 14, 33–38.

(60) Noguchi, Y.; Sugino, O.; Okada, H.; Matsuo, Y. First-Principles Investigation on Structural and Optical Properties of $M^{+}@C_{60}$ (Where M = H, Li, Na, and K). J. Phys. Chem. C 2013, 117, 15362–15368.

(61) Lu, T.; Chen, Q. Independent Gradient Model Based on Hirshfeld Partition: A New Method for Visual Study of Interactions in Chemical Systems. J. Comput. Chem. 2022, 43, 539–555.

(62) Jensen, F. Introduction to Computational Chemistry, John Wiley & Sons, West Sussex, 2017.

(63) Liu Z.; Wang, J.; Zhou, Q.; Lu, T.; Wang, X.; Yan, X.; Zhao, M.; Yuan, A. Size Dependence of Optical Nonlinearity for H-Capped Carbon Chains, H-(C≡C)*n*-H (*n* = 3-15): Analysis of Its Nature and Prediction for Long Chains. Phys. Chem. Chem. Phys. 2023, 25, 29165–29172.

(64) Liu, Z.; Lu, T. Optical Properties of Novel Conjugated Nanohoops: Revealing the Effects of Topology and Size. J. Phys. Chem. C 2020, 124, 7353–7360.

(65) Liu, Z.; Lu, T. Controllable Photophysical and Nonlinear Properties in Conformation Isomerization of Macrocyclic [32]Octaphyrin(1.0.1.0.1.0.1.0) Involving Hückel and Möbius Topologies. J. Phys. Chem. C 2020, 124, 845–853.

(66) Liu, Z.; Hua, S.; Wu, G. Extended First Hyperpolarizability of Quasi-Octupolar Molecules by Halogenated Methylation: Whether the Iodine Atom is the Best Choice. J. Phys. Chem. C 2018, 122, 21548–21556.

(67) Tuer, A.; Krouglov, S.; Cisek, R.; Tokarz, D.; Barzda, V. Three-Dimensional Visualization of the First Hyperpolarizability Tensor. J. Comput. Chem. 2011, 32, 1128–1134.

Table of Contents:

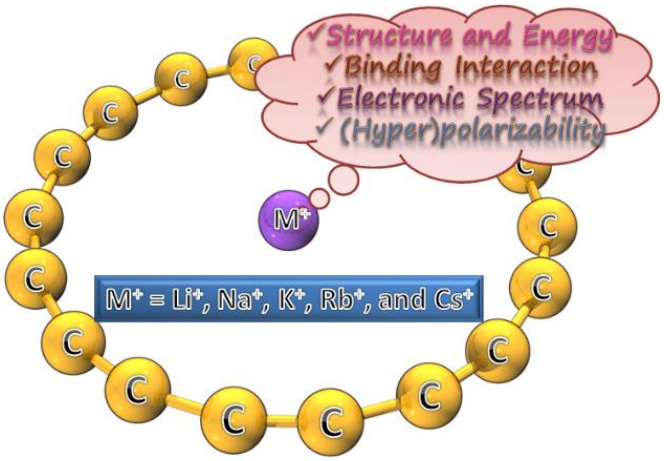

Synopsis:

The binding interaction between alkali-metal ions (M^+ = Li^+, Na^+, K^+, Rb^+, and Cs^+) and cyclo[18]carbon (C_{18}) as well as optical properties of stable endohedral complexes $M^+@C_{18}^{in}$ were carefully analyzed using accurate density functional theory (DFT) calculations. The similarities and differences in intramolecular interactions, electronic absorption spectra, and (hyper)polarizability of $M^+@C_{18}^{in}$ were then explored using advanced wavefunction analysis methods.